IOPscience iopscience.iop.org

Home Search Collections Journals About Contact us My IOPscience

Novel tri-modal defect structure in Nb-doped MOCVD Y $Ba_2Cu_3O_7$: a paradigm for pinning landscape control

This article has been downloaded from IOPscience. Please scroll down to see the full text article.

2012 Supercond. Sci. Technol. 25 095013

(http://iopscience.iop.org/0953-2048/25/9/095013)

View the table of contents for this issue, or go to the journal homepage for more

Download details:
IP Address: 128.219.49.14
The article was downloaded on 07/07/2012 at 01:38

Please note that terms and conditions apply.

Supercond. Sci. Technol. **25** (2012) 095013 (11pp) doi:10.1088/0953-2048/25/9/095013

Novel tri-modal defect structure in Nb-doped MOCVD $YBa_2Cu_3O_7$: a paradigm for pinning landscape control

Tolga Aytug[1], Victor A Maroni[2], Dean J Miller[2], Zhijun Chen[2], A Jeremy Kropf[2], Nestor J Zaluzec[2], Yuri Zuev[1], Eliot D Specht[1] and M Parans Paranthaman[1]

[1] Oak Ridge National Laboratory, Oak Ridge, TN 37831, USA
[2] Argonne National Laboratory, Argonne, IL 60439, USA

E-mail: aytugt@ornl.gov

Received 23 April 2012, in final form 20 June 2012
Published 6 July 2012
Online at stacks.iop.org/SUST/25/095013

Abstract
Immobilization of vortices, or flux pinning, is both an enduring scientific issue and one of the most important problems in optimizing high temperature superconductors (HTSs) for commercial use. Here, we demonstrate a practical approach to the creation of a multi-modal flux pinning landscape in $YBa_2Cu_3O_7$ (YBCO) films employing an industrially scalable metal–organic chemical vapor deposition technique. Through controlled additions of Nb, we have achieved a novel distribution of crystallographic defects that immobilize (pin) vortices in the YBCO matrix. That is, with only the addition of a single dopant element, a tri-modal, non-superconducting defect structure is induced that threads through the YBCO matrix laterally (parallel to the *ab* planes of YBCO), vertically (parallel to the YBCO *c*-axis), and isotropically in the form of random spherical defects. For optimally doped samples, the influence of these multi-modal nanocrystalline defect structures on the flux pinning properties manifests itself as a significant improvement in the critical current density (J_c) for all magnetic field orientations. The results demonstrate the possibility of achieving an ideal flux pinning landscape (from an orientation and strength viewpoint), which permits the design of HTS wires with fully-tunable properties by processes suitable for large-scale manufacturing.

(Some figures may appear in colour only in the online journal)

1. Introduction

The discovery and exploration of superconductivity in selected families of metal cuprates, inspired by the 1986 report of Bednorz and Mueller [1], has revolutionized thought about the practical application of superconductors in the electric power enterprise. The refinement of this discovery and exploration over some 25 years has led to the successful development and implementation of biaxially textured $MBa_2Cu_3O_7$ (or MBCO where M = Y or a rare earth element) in an epitaxial film format deposited on long lengths of templated metal strip [2–4], an embodiment that is nowadays referred to as the 'coated conductor'. Indeed, in today's market place, one can purchase 100 m lengths of coated conductor and there from fabricate transmission lines, motors, fault current limiters, high-field magnets, and related superconducting electric power devices [2–5]. The promise of the coated conductor (CC) is great but there are still pivotal issues that are related in large part to the cost/performance of the CC versus the industry standard—copper [6]. The principal issue evolves from the fact that the production cost of CC (expressed, e.g., in dollars per kilo-amp meter) is over an order of magnitude greater than that of conventional copper conductor. To bridge this cost/performance gap, and allow the CC to compete in an economically tenable manner with copper, means must be discovered to increase the current-carrying capability of the CC by at least an order of magnitude for all potential large-scale applications.

 © 2012 IOP Publishing Ltd Printed in the UK & the USA

A second closely related issue for near term applications of long-length CC is conductor performance in a magnetic field [7–10]. In devices with wound wire architectures (e.g., motors, generators, magnets) the induced field associated with current flow increases monotonically with increasing current. As the induced field approaches the critical field of the superconductor at a given temperature, a dissipative state arises wherein the driving force to move a vortex exceeds the pinning force, a partially resistive state develops, and the super-current falls off rapidly. It is well understood that the achievement of a high pinning force is centrally important to achieving strong flux pinning in magnetic fields of the magnitude anticipated in wound superconducting electric power devices (1–5 T).

Significant insight into the nature of the pinning characteristics of MBCO films is gained through measurements of the dependence of the critical current density (J_c) versus the angular orientation (θ) of the conductor with respect to the applied magnetic field (H). Measurements such as these, made as a function of field strength and temperature, allow the observer to evaluate the relative contributions of isotropic and anisotropic pinning centers, as shown, e.g., in the work of Maiorov *et al*, [8], Gutierrez *et al* [9], and MacManus-Driscoll *et al* [10].

Flux pinning in the MBCO superconductor is facilitated in all respects by the character of the defect structure within and adjacent to the MBCO lattice (also referred to hereinafter as the MBCO matrix). Maiorov *et al* [8], have provided a seminal discussion of how different types of defects within the MBCO matrix and random, often spherical, particles in contact with the MBCO matrix contribute to flux pinning in MBCO films. They refer to this collection of non-superconducting entities within and adjacent to the MBCO grains as the 'pinning landscape'. This pinning landscape can include (1) atomic level disorder in a small number of connected MBCO unit cells that suppresses superconductivity on the scale of a nanometer or less, which is generally at the level ascribed to point defects, (2) nano-scale spherical precipitates, (3) organized arrays of precipitates that tend to align either parallel to or perpendicular to the c-axis of the MBCO, and (4) splayed columnar defects with no preferential orientation (such as the defects produced by ion or neutron irradiation). They show that columnar defects contribute in a major way to the overall pinning energy, while nano-particles and splayed defects inhibit flux creep.

A most important feature is that the flux pinning is accomplished by defects on the nanometer scale that create a finite amount of non-superconducting space within the superconductor itself. So, clearly, the volume fraction of space allotted to flux pinning must be greater than zero but cannot be so great that it significantly diminishes the ability of the MBCO matrix to transmit super-current. The technical challenge is to achieve a level of microstructure control during film growth where one both optimizes the flux pinning landscape (from an orientation viewpoint) and maximizes the pinning force one gets from the non-superconducting space within the MBCO film.

Much of the work reported to date regarding flux pinning enhancement of MBCO films through microstructure control has been accomplished by film growth methods that involve pulsed laser deposition (PLD) of the MBCO [7, 8, 10]. While this work is important from a fundamental perspective, and has even been implemented on an industrial scale [11], one needs to recognize that the lowest-cost film growth methods employed for commercial fabrication of long-length conductor are based on chemical deposition methods, specifically metal–organic chemical vapor deposition (MOCVD) [2, 4] and chemical solution based metal–organic deposition (MOD) [3, 12]. In particular, the MOCVD-based technology developed and used by, e.g., SuperPower, Inc., has led to world record, long-length performance numbers for the MBCO CC [2]. The research reported herein is focused on achieving a multi-modal flux pinning landscape in MBCO films prepared by MOCVD. Accordingly, inspired by the work of Harrington *et al* [13] that revealed the formation of beneficial pinning architectures through group V transition metal (e.g., Nb and Ta) addition to PLD YBCO, we initiated research aimed at exploring flux pinning enhancement in MOCVD YBCO films containing controlled additions of Nb. A suitable available precursor for Nb was identified that was compatible with the standard Y:Ba:Cu mix used to deposit MOCVD YBCO films in our laboratory. YBCO films containing varying amounts of Nb were fabricated by deposition onto $LaMnO_3$/homo-epitaxial MgO/IBAD-MgO/Hastelloy tape [2, 14, 15] (referred to hereinafter as the substrate) in an experimental, reel-to-reel MOCVD chamber [14, 15], and a detailed characterization of the electrical, microstructural, and chemical properties was conducted.

2. Experimental details

YBCO films were produced using a custom-designed vertical, cold-wall, reel-to-reel MOCVD apparatus based on a liquid-source delivery system. The MOCVD depositions were made on $LaMnO_3$/IBAD-MgO templates [16] produced by SuperPower, Inc. The details of the prototype MOCVD system have been discussed in our previous publications [14, 15]. Essentially, a single source liquid precursor was prepared by dissolving solid metal–organic sources (specifically, the Y, Ba, Cu, and Nb salts of 2,2,6,6-tetramethylheptanedionate) in tetrahydrofuran with appropriately formulated molar ratios. The Y:Ba:Cu mole ratio was fixed at 1.3:2:2.6. Nb was added to the YBCO precursor mix in amounts ranging from 1 to 10 mol% relative to the Y content. The resulting solution was then transferred to the vaporizer by a liquid pump. The vaporized precursor was carried into the growth chamber by argon gas and mixed with oxygen before being injected into a showerhead above the heated substrate, which was continuously moving at a rate of $\sim$150 cm h^{-1}, to produce the 0.4–0.6 μm thick YBCO films examined in this work. The pressure in the reactor was adjusted to 2.5 Torr and the radiant heater temperature was maintained near 950 °C. This procedure enabled the study of variations/trends in structural properties and superconducting performance of YBCO films with respect to Nb content.

The electrical transport properties (T_c and J_c) of the fully processed films were measured using a conventional four-probe technique, with values of J_c assigned using a 1 μV cm^{-1} criterion. In-field transport measurements were performed at 77 K in a 1 T field.

Microstructural characterization was carried out in the Electron Microscopy Center at Argonne. Cross-sectional transmission electron microscopy (TEM) specimen preparation was carried out by focused ion beam (FIB) methods with samples extracted from the same regions used for transport measurements. TEM was carried out on an FEI Tecnai F20 equipped with an EDAX R-TEM Si(Li) energy dispersive detector. Spectrum imaging was carried out using a 4Pi analysis and control system.

The crystallography and phase content of the Nb-doped films were analyzed by x-ray diffraction (XRD). θ–2θ scans were measured in the Bragg–Brentano geometry using a Cu source operating at 50 kV and 100 mA and a Peltier-cooled energy dispersive Si(Li) detector tuned to Cu Kα. Samples were tilted for alignment with the YBCO (00L) reflections. Crystallographic phase and texture were analyzed using a 4-circle x-ray diffractometer employing the same Cu source and a bent graphite monochromator tuned to Cu Kα. The diffracted beam was collimated using 0.5° soller slits upstream of a NaI scintillation detector. The methodology used to interpret the XRD data is reported in detail elsewhere [14]. Briefly, the phase fractions of YBCO, Y_2O_3, and YBa_2NbO_6 were determined by comparing the integrated intensities of the YBCO(103) + (013), Y_2O_3(222), and YBa_2NbO_6(202) reflections. The structure factor for YBa_2NbO_6 was taken from Barnes *et al* [17] the others from Aytug *et al* [14]. Particle sizes were calculated using the Scherrer equation [18].

X-ray absorption spectroscopy (XAS) measurements in the Nb K-edge region were made on MRCAT beamline 10ID at Argonne's Advanced Photon Source. The beamline uses a cryogenically-cooled, double-crystal Si(111) monochromator to select the incident x-ray photon energy. Harmonic rejection and focusing to about 25 μm (in one dimension) was obtained using a dynamically bent Rh-coated mirror. The beam was incident upon the thin-film samples at a low angle, between 2° and 3°, to minimize the background signal from the substrate (which contains trace levels of Nb) by absorbing most of the beam within the deposited layers. Nb fluorescence from the MBCO samples was detected using a bent Laue analyzer tuned to the Nb Kα fluorescence line. For possible phase identification, single phase YBa_2NbO_6 and $BaNb_2O_6$ were used as Nb^{5+} standards which were prepared by a solid state reaction at 1150 °C for 36 h in air with several intermediate grindings and a final sintering at 1400 °C for 6 h starting from appropriate stoichiometric amounts of Y_2O_3, $BaCO_3$, and Nb_2O_5 powders. The purity of the synthesized phases was confirmed by powder XRD and subsequent comparison with published standard patterns.

Raman spectroscopy was used to gauge texture quality, detect and quantify lattice disorder effects, and probe for Cu-rich second phases (e.g., CuO and barium cuprates). Raman spectra were recorded using a Renishaw InVia Raman Microprobe equipped with a 633 nm He–Ne laser. The laser power density was maintained at a level well below 1 mW μm^{-2} to prevent thermal damage to the YBCO films. The sample handling and spectra processing procedures employed in this work have been discussed in prior publications [14, 19–21]. The through-thickness Raman measurements were facilitated by milling a surface-to-substrate crater through each YBCO film. This crater provided a tapered through-thickness slope along which the Raman spectra were collected. The preparation of the crater is done at low speed with a soft polishing tool that is lubricated as it polishes to prevent any heating that might lead to lattice atom migration. The Raman spectroscopy mainly identifies the phases present and the extent of cation disorder. We note that the phase chemistry and the cation disorder can only be changed if lattice atoms get moved around during polishing. Also, when we probe the top surface of the films away from the crater and the region of the slope near the top surface, the spectra look the same. More details on the method used to produce these craters were given in a previous publication [19]. All Raman spectra were recorded at ambient temperature.

3. Results and discussion

Shown in figure 1(a) are the angular dependences of J_c in an applied field of 1 T (77 K) for our baseline MOCVD YBCO films (Nb-free) and for MOCVD YBCO films containing 1, 2.5, 5, 7.5, and 10 mole per cent (mol%) Nb. Clearly the 1, 2.5, and 5 mol% Nb additions produce significant increases in J_c (1 T, 77 K) for all field angles, but beyond 5 mol% Nb the J_c falls off steadily to a point where the 10 mol% Nb sample exhibits a performance level below that of the baseline film. It is also noteworthy that doping with Nb has a significant effect on the self-field J_c [J_c (s.f.)] at 77 K, being a factor of ~2 higher for the 5 mol% film [J_c (s.f.) = 3.5×10^6 A cm^{-2}] relative to that of the undoped YBCO counterpart [J_c (s.f.) = 1.7×10^6 A cm^{-2}]. What is even more interesting is to compare the best performing Nb-added film (5 mol% Nb) with results obtained in our laboratory for Ce-, Ho-, and Zr-added MOCVD YBCO films, fabricated using the same substrate, the same MOCVD reactor and the same film deposition conditions [14, 15]. Figure 1(b) shows the angular dependent measurements of J_c (1 T, 77 K) Ce-, Ho-, and Zr-added films with the optimum composition for in-field performance (5 mol%, 10 mol%, and 5 mol%, respectively) together with the same plot for the 5 mol% Nb-added film shown in figure 1(a). During the measurements, the applied field was oriented at various angles with respect to the tape normal over a range of 180°. Note that the optimized Ce- and Ho-added films exhibit significantly superior J_c performance relative to the baseline film only around θ values corresponding to H being aligned parallel to the *ab* planes of the YBCO. In contrast, the optimized Zr-added film shows superior performance versus the baseline film primarily at orientations corresponding to H being aligned parallel to the *c*-axis of the YBCO (with some improvement in the minimum or 'floor level' J_c value as well). But most noteworthy in

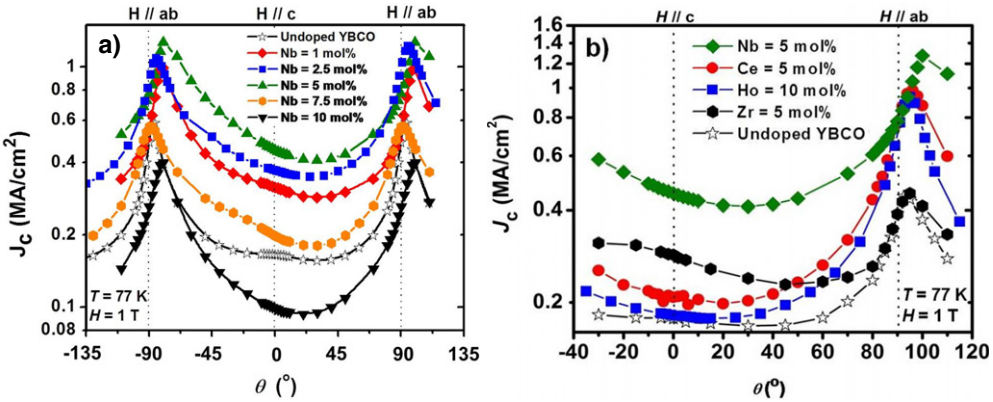

Figure 1. Critical current density angular dependence for YBCO films modified with various types and concentrations of dopants. (a) Angular dependence of J_c (θ) at 77 K and 1 T for films containing 1, 2.5, 5, 7.5, and 10 mol% Nb additions. (b) Comparison of the angular dependence of J_c for the baseline, undoped, YBCO film and films doped with 'optimum' levels of Nb, Ce, Ho, and Zr. Orientation angle of the field is relative to the YBCO *c*-axis direction.

figure 1(b) is the fact that the optimized Nb-doped film exhibits greatly enhanced J_c performance (versus baseline) at all values of θ. As we will show in the remainder of this paper, these distinctly different behaviors are unequivocally connected with the microstructure and chemistry associated with the respective metal atom additions to the MOCVD YBCO.

In our prior work on baseline MOCVD YBCO films and the corresponding Ce-, Ho, and Zr-added films [14, 15, 19], microstructural examinations by scanning electron microscopy (SEM) and TEM detected three different types of nano-precipitate landscapes, as follows: (1) the baseline MOCVD YBCO films typically exhibit a low-density, random distribution of small second-phase particles that are mostly Y_2O_3 (the fluorite phase). (2) The microstructure of the Ce- and Ho-added films is dominated by organized arrays of precipitates aligned parallel to the *ab* planes of the YBCO but also shows some evidence of random secondary phase nano-scale inclusions. The aligned precipitates and the random precipitates were mostly the Ce- or Ho-doped fluorite phase [14]. (3) The microstructure of the Zr-added films is also dominated by organized arrays of nano-precipitates that are aligned in a columnar fashion parallel to the *c*-axis of the YBCO; but in the case of Zr addition the precipitates are a $BaZrO_3$-like phase (BZO). Again, as in the other two cases, it was possible to detect some random, nano-scale, secondary phases [15, 19].

From these microstructural observations and the arguments presented by, e.g., Maiorov *et al* [8] and Gutierrez *et al* [9], a straightforward explanation for why the Ce- and Ho-added films show a distinct enhanced pinning effect near $H \parallel ab$ (relative to the baseline film) and why Zr-added films show a distinct enhanced pinning effect near $H \parallel c$ (again relative to the baseline film) is possible. In the simplest terms, the *ab* plane defects generated by Ce or Ho addition have a strong pinning capacity for magnetic field lines aligned near parallel to the *ab* planes of the YBCO, while the columnar defect arrays generated by Zr addition provide the strongest pinning for field lines parallel to the *c*-axis of the YBCO. Whereas this type of simple rationale generally explains the most obvious differences in the angular dependence of the J_c plot (figure 1(b)) for the baseline YBCO film and the Ce-, Ho-, and Zr-added films, as Maiorov *et al* [8] point out, the contributions to the overall pinning behavior from the various defect and precipitate types in the pinning landscape are not simply additive and can in some circumstances lead to opposing effects. Furthermore, it is not always possible to characterize or in some cases (e.g., point defects) even identify all the contributors to the overall pinning performance.

With this in mind, on the Nb-added MOCVD YBCO films (reported on in figure 1) we performed the same types of electron microscopy, XRD, Raman micro-spectroscopy, and synchrotron-based XAS measurements that we employed in our previous studies of Ce-, Ho-, and Zr-added YBCO films [14, 15, 19]. Typical results of TEM examination using full spectrum imaging are shown in figures 2 and 3 for the 10 mol% Nb-added sample. The three types of spectra that are most prevalent in the Nb-added samples are shown in figure 2(a). They signify the presence of three types of phase regions, one rich in Y, one containing Y together with Nb, and one (the most prevalent of all) that corresponds to the YBCO matrix. The spectral maps for Y, Nb, Ba, and Cu shown in figures 2(b)–(e), respectively, indicate (1) that the Y-rich phase exists in platelets parallel to the *ab* planes of the YBCO, (2) that an Nb-containing phase develops in pockets along the Y-rich plates and that both Y and Nb appear to be present together in these pockets, and (3) that the Ba exists predominantly in the YBCO matrix but shows some correlation with the Y–Nb pockets, suggesting the presence of a Y–Nb–Ba-containing phase. We note here that the Cu map is much like that of the Ba map except for the correlation in the Y–Nb–Ba pockets. In essence, we find the Ba and Cu to be predominantly in the YBCO matrix rather than in the precipitates and the discernible precipitates to be composed mainly of a Y-rich phase and a Y–Nb–Ba phase. In these maps the yellow arrows point to Y-rich domains and the white arrows point to Y–Nb–Ba domains.

What is not fully resolved in figure 2 is a more detailed view of Nb distribution in regions outside the Y–Nb–Ba pockets. To get a closer look at the Nb disposition, spectral

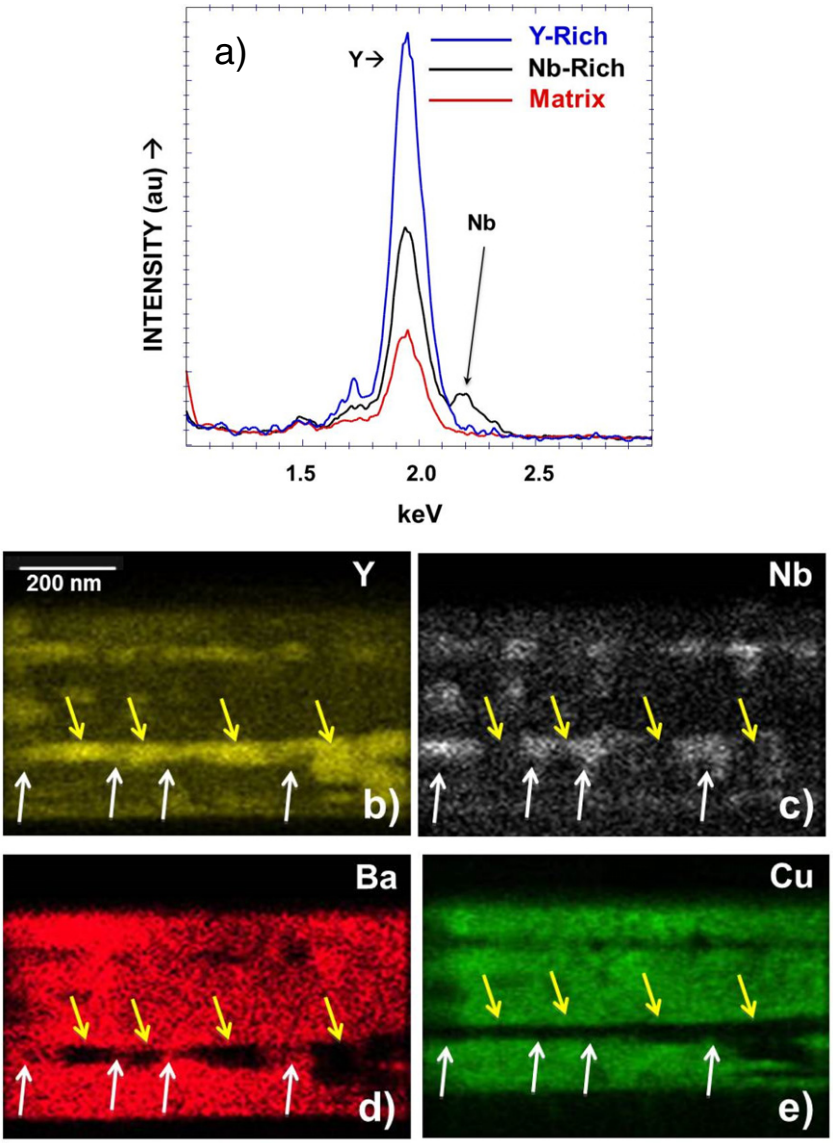

Figure 2. Spectral analysis obtained over a representative domain of a 10 mol% Nb-containing YBCO film. (a) Energy dispersive spectra obtained from three different phase regions: Y-rich, containing Y and Nb, and YBCO matrix. (b)–(e) Elemental maps for Y, Nb, Ba, and Cu, respectfully. Some of the Y-rich domains are marked by downward pointing yellow arrows and domains containing Y, Nb, and Ba are marked by upward pointing white arrows. The scale bar in image (b) applies to all images.

imaging was performed at a much higher level of resolution in these regions. The results of this high resolution imaging for the 10 mol% Nb-added sample are shown in figure 3. For better visualization of different phase domains in the film matrix, the Nb spectral map (figure 3(a)) is correlated with the maps obtained for Ba, Cu, and Y. These correlation maps are simply the superposition of two individual maps to help demonstrate spatial correlations more readily. In each image, the Nb spectral map is displayed in grayscale, individually in (a), with Ba as red in (b), with Cu as green in (c), and with Y as yellow in (d). The planar arrays of Y-rich phase interspersed with Y–Nb-containing pockets are again evident in the Nb map as well as in Y–Nb correlation image. More significantly, in these high resolution images we observe columnar strings of another type of Nb-containing precipitate. Unlike the case for planar precipitates, these columnar structures do not seem to contain Y, as illustrated in figure 3(d). Also apparent is the absence of a Cu signal coming from any segments of the planar or columnar arrays (figure 3(c)), offering evidence that Cu is not present in the phases that form these two defect structures. On the other hand, Ba appears to be present to some extent in both planar and columnar arrays (figure 3(b)). So, what is clear is that we have a case in which a single dopant element (Nb) is contributing to both planar and columnar array defects; and the formation of both defect types correlates well with the superior superconducting transport properties obtained for the Nb-added films, as discussed above for the results in figure 1.

Imaging of the 10 mol% Nb-added sample provided the clearest view of all three defect types induced by Nb additions. Spectral imaging of other samples confirms the nature of these defects. As an example, spectral imaging of the 5 mol%

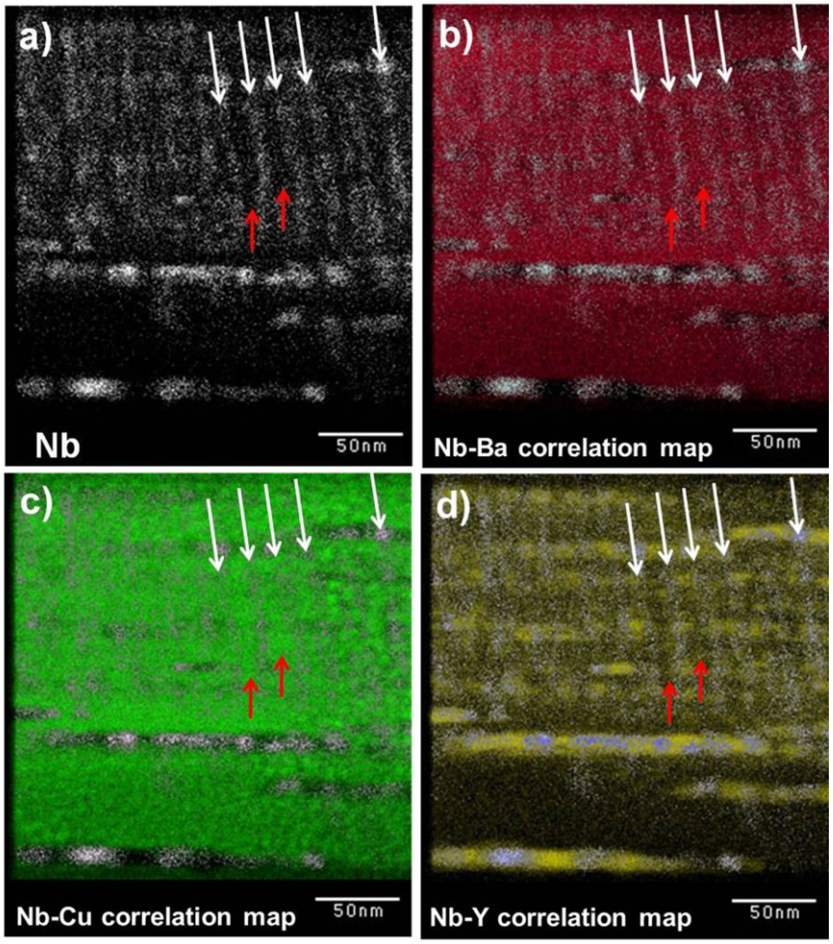

Figure 3. High resolution spectral images of a 10 mol% Nb-added MOCVD film. (a) Nb spectral map. (b)–(d) Correlation maps showing the relationship between (b) Nb–Ba, (c) Nb–Cu, and (d) Nb–Y. Some of the columnar defects are indicated by white arrows. Red arrows denote the regions in between the columnar arrays.

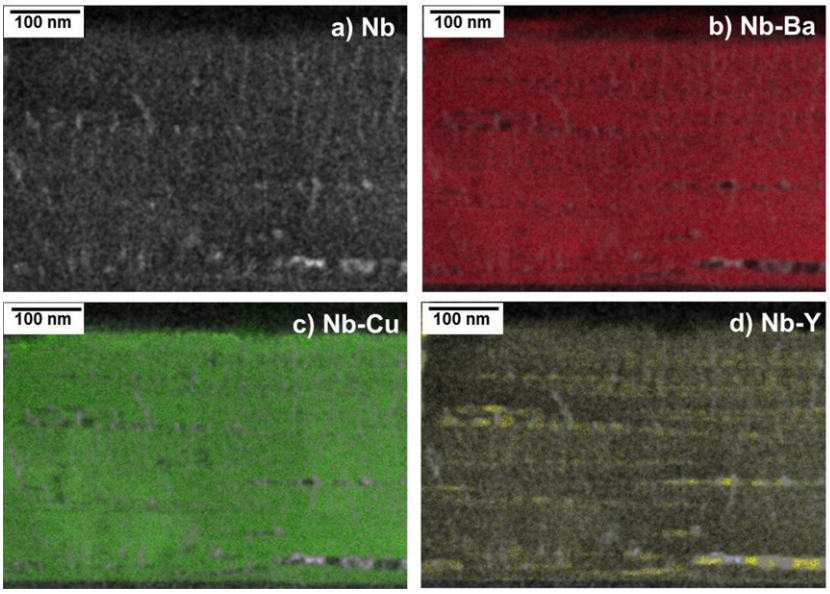

Figure 4. Spectral analysis from a 5 mol% Nb-added YBCO film. (a) Nb spectral map. Correlation maps showing the relationship between (b) Nb–Ba, (c) Nb–Cu, and (d) Nb–Y.

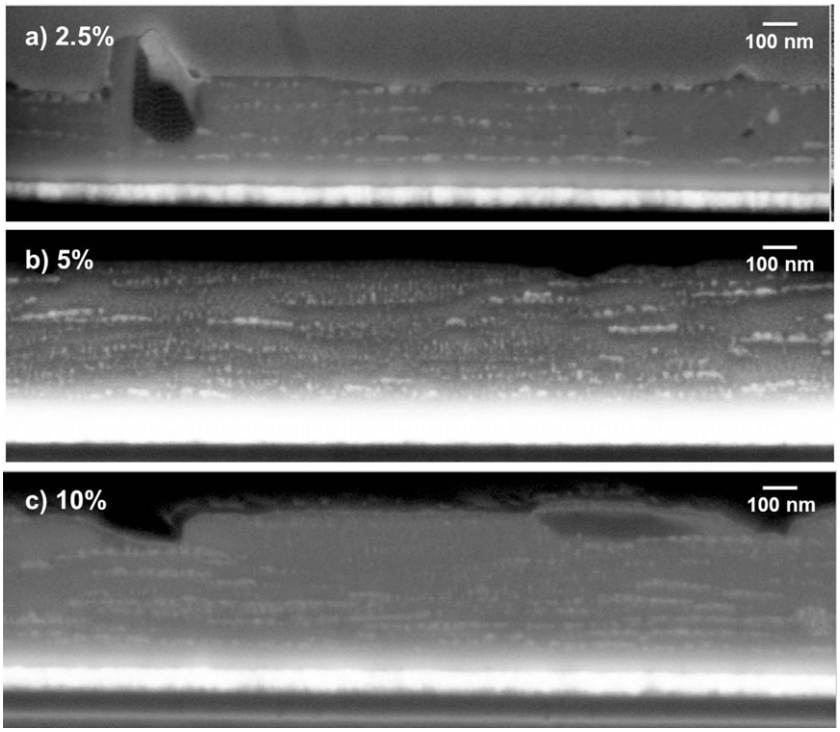

Figure 5. Scanning electron microscope images, from FIB-prepared cross-sections, of YBCO films modified with various concentrations of Nb. (a) 2.5 mol%, (b) 5 mol%, and (c) 10 mol%.

Nb-added sample is shown in figure 4. In this figure, the images are presented in the same manner as for figure 3. The individual defects are less distinctly delineated in these images, but Nb-rich columnar and planar defect arrays are clearly visible in figure 4(a), and from figures 4(b) and (c) it can be seen that they are anti-correlated with Y and Cu, but tend to be correlated with Ba, just as in the case shown in figure 3.

Another powerful view of this pinning landscape is provided by SEM. Figure 5 shows SEM from FIB-prepared cross-sections of 2.5, 5, and 10 mol% Nb-added samples. These images provide a more global view of defect structure and pinning landscape although it is important to note that they do not reveal the smallest defects or the columnar defects. However, a trend in defect structure that helps explain the changes in performance is apparent. At low Nb content (2.5 mol%, figure 5(a)), the defect content is rather low. At 5 mol% Nb (figure 5(b)), a highly refined and uniformly distributed defect structure is observed. At higher Nb content (10 mol%, figure 5(c)), the defect structure appears to be coarser and less uniformly distributed, instead aggregating into a higher density of planar defect arrays. This behavior is consistent with the trend observed in critical current as a function of Nb content.

In order to help establish the chemical form of these Nb-containing precipitates, whether those in the planar arrays are the same as (or different from) those in the columnar arrays, and whether there might be more to the pinning landscape in these Nb-added MOCVD YBCO films, we performed synchrotron-based XAS measurements on the Nb-added YBCO films. X-ray absorption spectra taken across the Nb K-edge region for the 2.5, 5, and 10 mol% Nb-added films are shown in figure 6(a), together with spectra for three reference phases—metallic Nb (serving as an Nb^0 standard), YBa_2NbO_6, and $BaNb_2O_6$. The latter two serve as Nb^{5+} standards and possible phase identifiers. The correspondence of the edge energy for the Nb-added films and the two Nb^{5+} standards in figure 6(a) clearly shows that the Nb is in the penta-valent state. It is also interesting that the Nb-added films and the $BaNb_2O_6$ exhibit a similar pre-edge feature, indicating that a phase analogous to $BaNb_2O_6$ could be present in the films.

To explore this further, the extended x-ray absorption fine structure (EXAFS) region of the spectra for the Nb-added films and the two Nb^{5+} standards was investigated. It was found that comparative Fourier transform (FT) fits of either one of the Nb^{5+} standards alone to the FTs for the Nb-added films gave poor results but a reasonable fit was obtained with a 50/50 mix of the two Nb^{5+} standards. The resulting fit of the FT magnitude versus radial coordinate is shown in figure 6(b). This fit does not necessarily confirm that phases with the exact compositions YBa_2NbO_6 and $BaNb_2O_6$ are the ones present in the Nb-added YBCO films. Rather it suggests that the Nb phases present in the YBCO films are structurally similar to these two niobate standards.

The YBa_2NbO_6 has a perovskite-like crystal structure [17] and the $BaNb_2O_6$ has a hexagonal structure with a distorted orthorhombic unit cell [22]. XRD examinations of the Nb-doped films revealed a perovskite-like phase with lattice parameter of 0.4233 ± 0.0003 nm and a particle size of 16 ± 3 nm as well as a fluorite-like phase with lattice parameter of 0.5312 ± 0.0002 nm and a particle

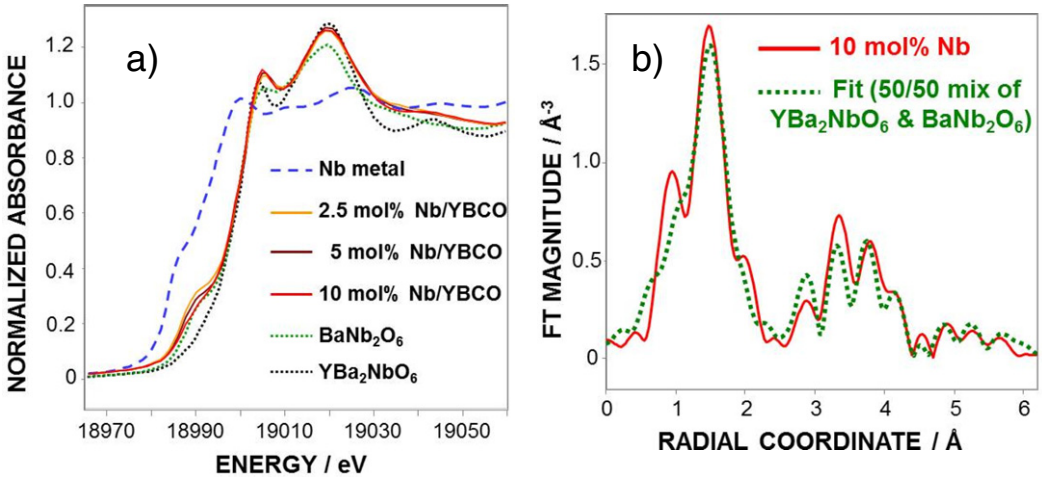

Figure 6. Synchrotron-based x-ray absorption spectral measurements. (a) Normalized x-ray absorption spectra in the Nb K-edge region for the MOCVD films containing 2.5, 5 and 10 mol% Nb additions. Spectra for an Nb metal foil, YBa_2NbO_6, and $BaNb_2O_6$ are also included for comparison purposes. (b) EXAFS Fourier transforms (radial coordinate plots) for the 10 mol% Nb-added film and a 50/50 mix of the YBa_2NbO_6, and $BaNb_2O_6$ standards.

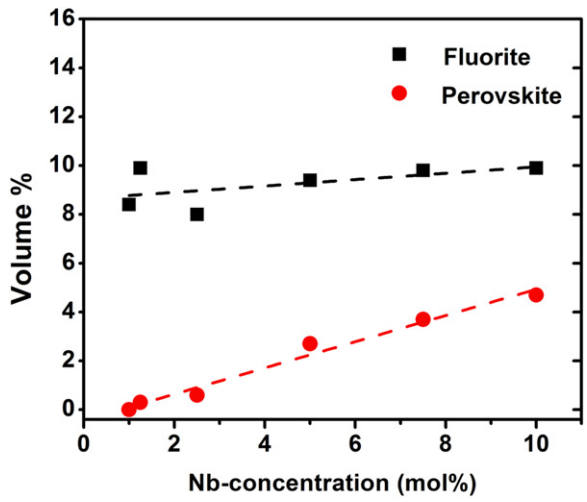

Figure 7. Variation of perovskite and fluorite phase volume fractions in MOCVD YBCO films as a function of Nb doping level. Dashed lines are linear fits to data.

size of 16 ± 1 nm. XRD shows no evidence of $BaNb_2O_6$ or a related Nb-containing hexagonal phase type, perhaps because the crystallites are very small, the reflections are weak, and/or the volume fraction of this particular phase type is too low. The lattice parameter of the perovskite-like phase is close to 0.422 03 nm, the perovskite subcell lattice parameter for YBa_2NbO_6 [17], while the lattice parameter of the fluorite phase is close to 0.5302 nm, the fluorite subcell lattice parameter of Y_2O_3. Phase volume fraction estimates based on the XRD data (figure 7) revealed that while the volume fraction of the perovskite-like phase increases linearly with increasing Nb addition, the fluorite-like phase fraction increases only slightly.

To further understand how the added Nb reacts during the MOCVD process through which the YBCO forms, what phases the Nb actually ends up being a constituent of, and whether/how Nb-containing phases influence the YBCO flux pinning landscape, we performed several other types of measurements. First of all, we observed that over the full range of Nb additions (0–10 mol%) the critical temperature (T_c) of the films ranged from 88 to 91 K. In fact, T_c was 90 K for the baseline (0 mol% Nb) film, 91 K for the best performing sample (5 mol% Nb), and 88 K for the most heavily doped sample (10 mol% Nb). This small variation of T_c over a wide range of additive composition strongly suggests that very little (if any) Nb enters the YBCO matrix, e.g., as a substitute for Y, Ba, or Cu. A similar conclusion was reached by Ercolano *et al* [23] in their work on Nb-doped PLD YBCO.

Raman spectroscopy has proven to be a useful examination method for probing the extent to which additive elements influence the lattice ordering of MBCO films (and consequently T_c) [20, 21]. The portion of the Raman spectra obtained for the 0, 1, 5, and 10 mol% Nb-added YBCO films shown in figure 8(a) provides information about the extent to which Nb addition influences the cation disorder level (C-Dis) of the YBCO and the amount of Ba–Cu–O phase formation. The spectral intensities in figure 8(a) have been normalized to the 450 cm^{-1} O2+/O3+ mode of YBCO [20]. The best way to appreciate the results in figure 8(a) is through a comparison with similar results for the Ce-, Ho-, and Zr-added films we reported on previously [14, 15, 19]. The bar graph in figure 8(b) compares the relative extents of cation disorder and Ba–Cu–O phase formation (normalized with respect to the intensity of the 450 cm^{-1} phonon mode of YBCO) measured for the optimum performing film for each additive element. The graph reveals that (1) the Ba–Cu–O levels exhibit a two- to three-fold elevation compared to the baseline YBCO film for all four additive elements, (2) Ce, Ho, and Zr additions also tend to increase the cation disorder level by two- to three-fold, but (3) Nb addition appears to produce a cation disorder level no greater than that of the baseline film. Prior studies of the relationship between this cation disorder effect and flux pinning performance have shown that a certain amount of

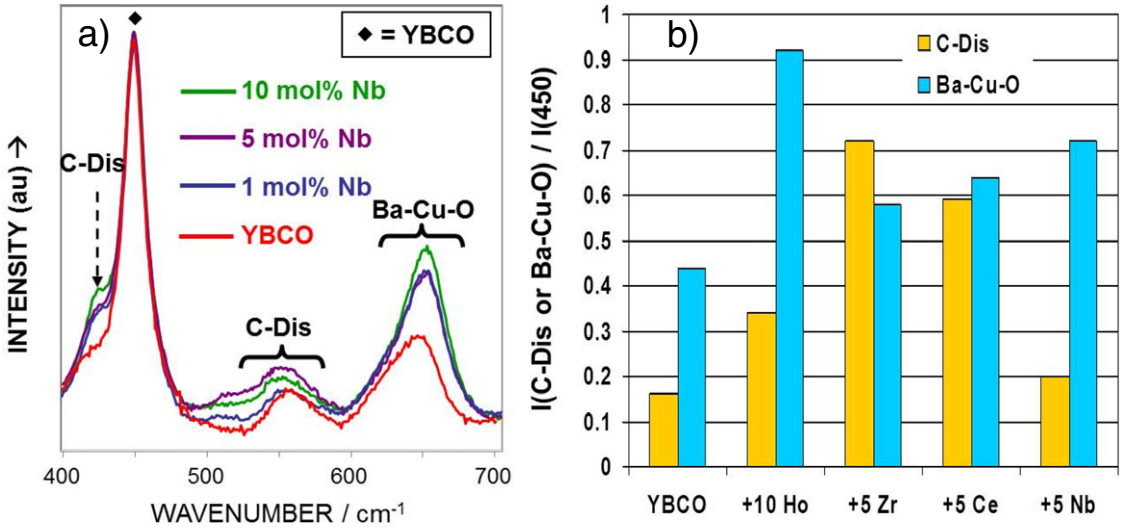

Figure 8. Raman spectroscopy of the Nb-added films. (a) Comparison of the normalized average through-thickness Raman spectra for the 1, 5, and 10 mol% Nb-added samples together with the spectrum of an undoped MOCVD YBCO film. The diamond symbol denotes the 450 cm^{-1} O2+/O3+ mode of tetragonal YBCO. (b) Comparison of the relative extents of cation disorder and Ba–Cu–O phase (determined by ratioing of respective integrated band intensities with the integrated band intensity of the 450 cm^{-1} band of YBCO using the same type of methodology described previously [19]) for the undoped and doped films with 'optimum' levels of Ho, Zr, Ce, and Nb.

cation disorder is actually beneficial to flux pinning in the case of PLD films [21], but this 'optimum' amount has not been firmly ascertained. What is known is that continuously increasing cation disorder is not beneficial and in fact becomes detrimental beyond a certain level. In a sense, the collective cation disorder probably acts like an array of distributed point defects, but too much cation disorder means too many unit cells of the YBCO matrix get compromised and current path continuity begins to degrade.

Returning our attention to figure 1(b), we can now address the behavior of the Nb-added MOCVD YBCO film in comparison with the baseline film and the Ce-, Ho-, and Zr-added films. To put this in perspective, we show in figure 9(a) a representative TEM image revealing the typical defect structures in Nb-added films. In this image one can find examples of the planar precipitate arrays and the columnar precipitate arrays identified in figures 2 and 3, and in addition isolated, randomly located nano-scale spherical precipitates that are also common to the Nb-added films. These three defect types coupled with the implied presence of cation-disorder-related point defects in the YBCO matrix comprise what we can reasonably discern about the pinning landscape of the Nb-added films from the results presented herein. With this landscape we have defects that provide stronger pinning for $H \parallel ab$, stronger pinning for $H \parallel c$, and isotropic pinning of a kind that should tend to lift the 'floor level' J_c for all values of θ.

Figure 9(b) summarizes the dominant pinning microstructure, the identified dopant-containing phase(s), and the relative extent of Raman-determined lattice disorder for the optimum performing Ce-, Ho-, Zr-, and Nb-added films as shown in figure 1(b). Note again it is only the Nb-film that contains all three types of defect structures. Also note again that the Nb-added film exhibits the lowest level of cation disorder—a level comparable to that of the baseline MOCVD YBCO film as indicated in figure 8(b). It therefore appears that Nb addition to YBCO produced by the MOCVD process has the capability to induce a tri-modal defect structure that threads through the YBCO matrix laterally (parallel to the *ab* planes of YBCO), vertically (parallel to the YBCO *c*-axis), and isotropically in the form of random spherical defects (quite likely the fluorite phase detected by XRD). This happens without detrimental increase in the extent of cation disorder within the YBCO unit cell structure. And all this comes about with only the addition of a single element—Nb.

4. Perspective on Nb addition to MBCO

Our present study is not the first to investigate the effect of Nb addition or substitution on the superconducting properties of MBCO, but it is the first to provide an observation of the unique multi-modality possible with Nb addition to MOCVD YBCO. It is also the first to demonstrate this approach for a commercially scalable process. In recent years there have been several reports of enhanced pinning in Nb-added MBCO produced by PLD methods [23–28]. Ercolano *et al* [23] reported a two-fold improvement in J_c for $H \parallel c$ in YBCO/YBa_2NbO_6 composite PLD films and also evidence of some improvement in J_c over a relatively large angular range (similar in magnitude to the findings of the present MOCVD work). They attributed this enhanced pinning (relative to undoped YBCO) to non-superconducting YBa_2NbO_6 nano-rods aligned with the YBCO *c*-axis, as detected by TEM. Kai *et al* [24, 25] conducted similar studies of PLD ErBCO doped with either $BaNb_2O_6$ or $ErBa_2NbO_6$. In both cases they observed improved flux pinning for $H \parallel c$ which they too attributed to MBa_2NbO_6-type nano-rods aligned with the YBCO *c*-axis (again detected by TEM). Reich *et al* [26] prepared PLD films using YBCO/$Y_2Ba_4CuNbO_y$ targets. In a similar vein to the findings of Ercolano *et al* and Kai *et al*,

a)

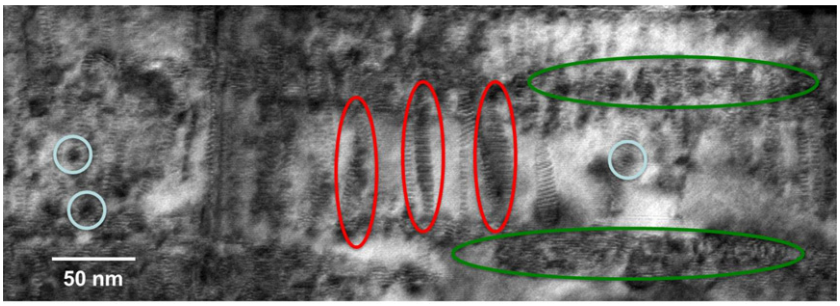

b)

Dopant	Optimum mol%	Spherical Precipitates	ab-Planar Arrays	Columnar Defects	Dopant-Containing Phases	Lattice Disorder
Zr	5			✓	$BaZrO_3$	High (3X)
Ce	5	✓	✓		$(Y,Ce)_2O_3$	High (3X)
Ho	10	✓	✓		$(Y,Ho)_2O_3$ (Y,Ho)BCO	Moderate (2X)
Nb	5	✓	✓	✓	YBa_2NbO_3 $BaNb_2O_6$(?)	Low (X)

Figure 9. Microstructure of a 10 mol% Nb modified sample. (a) TEM micrograph showing various defect structures present in these films. Some of the planar and columnar precipitates are highlighted with ovals and some spherical precipitates are outlined with circles. (b) Tabulated summary of dominant defect structures and phases, along with lattice disorder for MOCVD YBCO films modified with 'optimum' levels of Zr, Ce, Ho, and Nb additions.

they attributed the rather modest improvement they observed in the irreversibility field (relative to undoped YBCO) to *c*-axis correlated defects, which they surmised from XRD studies to be a phase best represented by the composition $Y_{2-x}Ba_2Nb_xO_6$. Wee *et al* [27] also reported the observation of columnar defects in PLD YBCO films that were prepared by Nb-coablation. The defects were composed of self-aligned YBa_2NbO_6 nano-rods parallel to the *c*-axis of the YBCO lattice. Grekhov *et al* [28] prepared an Nb-doped YBCO target which they laser ablated on to a variety of substrates and then used the Nb-doped layer as the template for PLD YBCO film growth. They determined that the Nb-doped YBCO layer exhibited a unique superconductor–insulator behavior. However, none of these PLD studies specifically identify corresponding lateral defect structures or pay much attention to random, through-film spherical precipitates.

Numerous others have tried to dope bulk MBCO with various chemical forms of Nb (e.g., Nb_2O_5, NbO_2, YBa_2NbO_6, etc). The bulk processing methods used have ranged from solid state reaction sintering, to melt texturing, to thermolysis. The work of Muralidhar *et al* [29], Yeoh *et al* [30], Abdullah and Tan [31], and Strukova *et al* [32] report examples of such studies and give references to relevant prior research. In virtually all cases, some improvement is seen in J_c, particularly at higher magnetic fields, when the Nb is added. Where the form of the Nb-containing phase(s) has been investigated, it is almost always present as random nano-precipitates as opposed to ordered planar and/or columnar arrays of correlated defects. There is also very little evidence in any of the previously published work to indicate that Nb enters the MBCO lattice to a detectable extent.

5. Summary

In summary, we have demonstrated the creation of a multi-modal flux pinning landscape in YBCO films with only a single dopant element (Nb) using an industrially scalable fabrication process, i.e., metal–organic chemical vapor deposition. Specifically, we show that this landscape encompasses at least three types of ideal nano-sized defect structures in the YBCO matrix (lateral, vertical and spherical) and as such provides significant improvement in flux pinning that yields films with enhanced current-carrying capability for all magnetic field orientations. The results offer a practical path forward for commercial high temperature superconductor wire production with fully tunable flux pinning properties.

Acknowledgments

The support and encouragement of Venkat Selvamanickam at the University of Houston and Yimin Chen of SuperPower, Inc, are greatly appreciated. The research described in

this paper was sponsored by the US Department of Energy (USDOE), Office of Electricity Delivery and Energy Reliability, Advanced Cables and Conductors. Use of instrumentation at Argonne's Electron Microscopy Center, Center for Nano-scale Materials, and Advanced Photon Source was supported by the USDOE, Office of Science, Office of Basic Energy Sciences. This research was performed at the Oak Ridge National Laboratory under contract DE-AC05-00OR22725 between UT-Battelle, LLC and the USDOE, and at the Argonne National Laboratory under contract DE-AC02-06CH11357 between UChicago Argonne, LLC and the USDOE.

Author contributions

TA carried out the deposition of films, initial structural characterizations, data analysis, and manuscript preparation. VAM worked in manuscript preparation, data analysis, and together with ZC conducted Raman spectroscopy measurements. YZ carried out the transport measurements and EDS analyzed the crystallography and phase content of the films. MPP prepared the precursor solutions. DJM contributed to manuscript preparation and together with NJZ performed microstructural examinations by TEM and STEM as well energy dispersive spectroscopy with elemental mapping and spectral imaging of the defect structures. AJK carried out x-ray absorption spectroscopy measurements.

References

[1] Bednorz J G and Müller K H 1986 Possible high T_c superconductivity in the Ba–La–Cu–O system *Z. Phys.* B **64** 189–93

[2] Selvamanickam V and Dackow J 2010 *2010 DOE Advanced Cables and Conductors Peer Review* www.htspeerreview.com/pdfs/presentations/day%201/joint/2J_Progress_in_SuperPowers_2G_HTS_WireDevelopmentandManufacturing.pdf

[3] Fleshler S *et al* 2009 Scale-up of 2G wire manufacturing at American Superconductor Corporation *Physica* C **469** 1316–21

[4] Shiohara Y, Fujiwara N, Hayashi H, Isumi T and Yoshizumi M 2009 Japanese efforts on coated conductor processing and its power applications: new 5 year project for materials and power applications of coated conductors (M-PACC) *Physica* C **469** 863–7

[5] Farrell R 2010 *High Temperature Superconducting Underground Power Cable: The Albany Cable Project Final Report* www.osti.gov/bridge/purl.cover.jsp?purl=/975691-IRpM7i/

[6] Maroni V A 2007 Future of high-critical-temperature superconducting ceramics *Am. Ceram. Soc. Bull.* **86** 29–33

[7] Matsumoto K and Mele P 2010 Artificial pinning center technology to enhance vortex pinning in YBCO coated conductors *Supercond. Sci. Technol.* **23** 014001

[8] Maiorov B *et al* 2009 Synergetic combination of different types of defect to optimize pinning landscape using $BaZrO_3$-doped $YBa_2Cu_3O_7$ *Nature Mater.* **8** 398–404

[9] Gutiérrez J *et al* 2007 Strong isotropic flux pinning in $YBa_2Cu_3O_{7-x}$–$BaZrO_3$ films derived from chemical solutions *Nature Mater.* **6** 367–73

[10] MacManus-Driscoll J L *et al* 2010 High current, low cost YBCO conductors—what's next? *Supercond. Sci. Technol.* **23** 034009

[11] Fuji H, Igarashi M, Hanada Y, Miura T, Hanyu S, Kakimoto K, Iijima Y and Saitoh T 2008 Long Gd-123 coated conductor by PLD method *Physica* C **468** 1510–3

[12] Zalamova K, Pomar A, Palau A, Puig T and Obradors X 2010 Intermediate phase evolution in YBCO thin films grown by the TFA process *Supercond. Sci. Technol.* **23** 014012

[13] Harrington S A 2009 Self-assembled, rare earth tantalate pyrochlore nanoparticles for superior flux pinning in $YBa_2Cu_3O_{7-\delta}$ films *Supercond. Sci. Technol.* **22** 022001

[14] Aytug T *et al* 2011 Nano-engineered defect structures in Ce- and Ho-doped metal–organic chemical vapor deposited $YBa_2Cu_3O_{6+\delta}$ films: correlation of structure and chemistry with flux pinning performance *J. Appl. Phys.* **109** 113923

[15] Aytug T *et al* 2010 Enhanced flux pinning in MOCVD-YBCO films through Zr additions: systematic feasibility studies *Supercond. Sci. Technol.* **23** 014005

[16] Xiong X M *et al* 2009 Progress in high throughput processing of long-length, high quality, and low cost IBAD MgO buffer tapes at SuperPower *IEEE Trans. Appl. Supercond.* **19** 3319–22

[17] Barnes P W, Lufaso M W and Woodward P M 2006 Structure determination of A2M(3+)TaO6 and A2M(3+)NbO6 ordered perovskites: octahedral tilting and pseudosymmetry *Acta Crystallogr.* B **62** 384–896

[18] Cullity B D and Stock S R 2001 *Elements of X-ray Diffraction P-70* (Upper Saddle River, NJ: Prentice-Hall)

[19] Maroni V A, Kropf A J, Aytug T and Paranthaman M 2010 Raman and x-ray absorption spectroscopy characterization of Zr-doped MOCVD YBCO *Supercond. Sci. Technol.* **23** 014020

[20] Venkataraman K, Baurceanu R and Maroni V A 2005 Characterization of $MBa_2Cu_3O_{7-x}$ thin films by Raman microspectroscopy *Appl. Spectrosc.* **59** 639–49

[21] Maroni V A, Li Y, Feldmann D M and Jia Q X 2007 Correlation between cation disorder and flux pinning in the $YBa_2Cu_3O_7$ coated conductor *J. Appl. Phys.* **102** 113909

[22] Galasso F, Layden G and Ganung G 1968 ANb_2O_6 and ATa_2O_6 phases *Mater. Res. Bull.* **3** 397–408

[23] Ercolano G *et al* 2010 Enhanced flux pinning in $YBa_2Cu_3O_{7-\delta}$ thin films using Nb-based double perovskite additions *Supercond. Sci. Technol.* **23** 022003

[24] Kai H *et al* 2009 Influence of growth temperature on microstructure and superconducting proprties of $ErBa_2Cu_3O_{7-\delta}$ films with $Ba(Er_{0.5}Nb_{0.5})O_3$ nanorods *IEEE Trans. Appl. Supercond.* **19** 3435–8

[25] Kai H *et al* 2008 Effects of growth temperature for superconducting properties and microstructures of PLD-$ErBa_2Cu_3O_{7-\delta}$ film with $BaNb_2O_6$ *Physica* C **468** 1854–7

[26] Reich E *et al* 2009 Structural and pinning properties of $Y_2Ba_4CuMO_y$ (M = Nb, Zr)/$YBa_2Cu_3O_{7-\delta}$ quasi-multilayers fabricated by off-axis pulsed laser deposition *Supercond. Sci. Technol.* **22** 105004

[27] Wee S H *et al* 2010 Formation of self-assembled, double perovskite, Ba_2YNbO_6 nanocolumns and their contribution to flux pinning and J_c in Nb-doped $YBa_2Cu_3O_{7-\delta}$ films *Appl. Phys. Express* **3** 023101

[28] Grekhov I *et al* 1997 A new buffer layer for high-quality HTSC ultrathin film fabrication *Physica* C **276** 18–24

[29] Muralidhar M *et al* 2009 Observation of record flux pinning in melt-textured NEG-123 superconductor doped by Nb, Mo, and Ti nanoparticles *Physica* C **469** 1196–9

[30] Yeoh W K *et al* 2009 Improved flux pinning in Y–Ba–Cu–O superconductors containing niobium oxide *IEEE Trans. Appl. Supercond.* **19** 2970–3

[31] Abdullah M H and Tan B T 1995 Superconducting properties of Nb-doped Y–Ba–Cu–Nb–O superconductors *Solid State Commun.* **93** 93–6

[32] Strukova G K *et al* 1993 Effect of Nb doping on properties of Y–Ba–Cu ceramics *Supercond. Sci. Technol.* **22** 589–92